Springer Verlag, (2018)
Spectroscopic Ellipsometry for Photovoltaics pp 201-225

10.1007/978-3-319-75377-5_8

Chapter 8
Crystalline Silicon Solar Cells

Gerald E. Jellison Jr. and Pooran C. Joshi

Abstract Most solar cells are fabricated from crystalline or semicrystalline silicon since they are relatively inexpensive starting materials and the resulting solar cells are very efficient. As a result, the optical properties of silicon are extremely important in many aspects of solar cell manufacture, and have been determined by many groups using several techniques. The most reliable values of the optical functions of silicon have been determined using spectroscopic ellipsometry, augmented by optical transmission measurements of the absorption coefficient for wavelengths greater than 700 nm. Obviously, these optical functions depend on the wavelength of light, but they also depend significantly on temperature and morphology. Several thin films are very important to solar cell manufacture, including silicon nitride, silicon dioxide, and aluminum oxide. While the optical properties of these thin films are strong functions of deposition conditions, spectroscopic ellipsometry is ideal for characterizing them. This work will present recent spectroscopic ellipsometry data and optical transmission data from which the optical functions of silicon are obtained. The optical transmission data have been fit from 700 to 1200 nm to a modification of Macfarlane's et al. formula [Phys. Rev. 111, (1958) 759], resulting in a reduced χ^2 of 0.84. This formulation is particularly valuable in that it gives the optical absorption coefficient from 700 to 1200 nm as a function of both wavelength and temperature.

8.1 Introduction

Elemental silicon (atomic number 14) is the 2nd most abundant element in the earth's crust (28% by mass), following only oxygen (46% by mass). It is most often found in nature bonded to oxygen and a variety of other elements to form various

G. E. Jellison Jr. (✉) · P. C. Joshi
Oak Ridge National Laboratory, Oak Ridge, TN 37830, USA
e-mail: jellisongejr@ornl.gov

P. C. Joshi
e-mail: joshipc@ornl.gov

© Springer International Publishing AG, part of Springer Nature 2018

H. Fujiwara and R. W. Collins (eds.), *Spectroscopic Ellipsometry for Photovoltaics*,
Springer Series in Optical Sciences 212,
https://doi.org/10.1007/978-3-319-75377-5_8

silicates. Using a variety of chemical and thermal treatments, silicon can be separated from oxygen and other elements to make a very pure material with impurity concentrations less than one part in a billion (9 N purity). Using a variety of crystal growth techniques, this material can be grown into nearly perfect single crystals (mono-crystalline silicon) or using less expensive techniques, grown into semi-crystalline silicon with grain sizes ~1 mm in diameter. Mono-crystalline silicon can be produced as less-pure, less expensive solar grade silicon or as electronic grade silicon, which is of much higher purity, more expensive, but is useful for the greater electronics industry. Solar cells made from multi-crystalline silicon will have efficiencies up to ~22%, while 25% single junction monocrystalline silicon solar cells have been made from electronic grade silicon.

Above 1414 °C, silicon is liquid. While crystalline silicon is semiconducting, liquid silicon is metallic and very reactive with air. Like water (and unlike most other materials), liquid silicon is denser than the solid. This characteristic means that solid silicon will float on liquid silicon, making crystal growth much easier.

Crystalline silicon has the cubic diamond structure, where each silicon atom is bonded to 4 other silicon atoms forming a perfect tetrahedron. The diamond lattice is highly symmetric with a point group m3m (O_h Schönflies) and space group number 227 (Fd-3m). Therefore, the optical properties of silicon are isotropic. At room temperature, photons greater than ~1.05 eV are absorbed; according to the Shockley-Queisser limit [1] the maximum possible efficiency of a single-junction silicon solar cell is ~31.5%. The fundamental band edge of silicon is indirect; that is, photon absorption requires the absorption or the emission of a phonon to excite an electron from the valence band to the conduction band. This is both good and bad for photovoltaics. It is good because electron-hole recombination is much less likely, dramatically increasing the minority carrier lifetime and diffusion length. In silicon, the minority carrier lifetime is primarily determined by impurities and defects in the material, which act as recombination centers. These centers can trap either a free electron from the conduction band or a free hole in the valence band, which then can be recombined with a free hole or free electron. The bad part is that the indirect gap and resultant requirement that a phonon be either generated or absorbed also results in a much less efficient light absorption process. As a result, many photo-generated electron-hole pairs are created much deeper into the material than for direct gap materials, which must then diffuse to the junction to be collected. Much of the recent work in silicon photovoltaics has focused on minimizing the bad (long penetration depth) and maximizing the good (long minority carrier lifetime), resulting in gradually improving efficiencies over time.

In this chapter, we will discuss the optical properties of silicon and related materials. While ellipsometry has been the technique of choice for much of this work, it has not been the only choice, so we will also discuss these other techniques as appropriate. Since the primary interest in this book is the application of ellipsometry to photovoltaics, we will focus on the optical properties from 200 to 1200 nm. While there is very little sunlight in the spectral region 200–350 nm that reaches the earth, this spectral region contains interesting insights into silicon and

related materials, and is used in many diagnostics for photovoltaics, so this region is discussed as well.

8.2 Optical Properties of Silicon: UV to Near IR (200–1200 nm)

The linear optical functions of an isotropic material can be expressed as either the complex refractive index $N(\lambda)$ or the dielectric function $\varepsilon(\lambda)$. The two are related by

$$\varepsilon(\lambda) = \varepsilon_1 - i\,\varepsilon_2 = N(\lambda)^2 = (n(\lambda) - ik(\lambda))^2 \tag{8.1}$$

where the real and imaginary parts of the dielectric function are given by ε_1 and ε_2, n is the refractive index and k is the extinction coefficient. The wavelength λ is related to the photon energy E (eV) = 1239.8/λ (nm). Since silicon is an isotropic material, the dielectric function is a scalar, requiring only a single complex quantity at each wavelength. The optical functions are directly related to the normal incidence reflectivity R (where there is no surface over layer) and is given by

$$R = \frac{(n-1)^2 + k^2}{(n+1)^2 + k^2}. \tag{8.2}$$

The optical absorption coefficient α is given by

$$\alpha = \frac{4\pi k}{\lambda}, \tag{8.3}$$

where the fraction of light not absorbed at a depth d into the material is given by $f = \exp(-\alpha d)$.

8.2.1 Measurement Techniques

The earliest measurements of the optical properties of single-crystal silicon were performed using specular reflectivity, transmission, and minimum deviation [2–11]. Specular reflectivity measurements are relatively simple to perform and can be done in vacuum, making it possible to do these measurements at high photon energies ($E > 6$ eV corresponding to $\lambda < 200$ nm). However, reflectivity measurements suffer from two disadvantages. First of all, the optical functions are not determined directly from the reflectivity measurements, but must be calculated using Kramers-Kronig integration. This integration requires reflectivity data in the energy range from 0 to ∞, which does not exist, so extrapolations beyond the measured data are required. Secondly, reflected light that is not collected by the detector (such

as scattered light) will result in a lower reflectivity, distorting the final result. Specular transmission measurements can be converted directly into the optical absorption coefficient α using the expression for the internal transmission T (correcting for reflection and non-specular losses)

$$T = \exp(-ad), \tag{8.4}$$

where d is the thickness of the sample. Transmission is particularly useful for wavelengths where the light penetration is large; with silicon, this occurs for wavelengths $\lambda > \sim 700$ nm. Transmission gives no information concerning the refractive index. Minimum deviation measurements require that the sample be transparent and that the sample can be constructed as a prism with well-polished faces. For silicon, this technique can only be used in the infrared range with $\lambda > \sim 1200$ nm.

Recently, spectroscopic ellipsometry has become an important technique for the determination of the optical functions of silicon. For ellipsometric measurements, polarized light is reflected from the sample surface, which changes the polarization state of the light. The resulting polarization state is then analyzed to characterize the change in the polarization state generated by the sample. (This is discussed in Chap. 2.) For an isotropic sample, the measured ellipsometric parameters can be expressed in several different ways. The fundamental measured quantity is complex ρ:

$$\rho = (\rho_r + i\rho_i) = \frac{r_p}{r_s} = \frac{C + iS}{1 + N} = \tan(\psi)e^{i\Delta}. \tag{8.5}$$

The complex reflection ratios r_p and r_s are for p- and s-polarized light, (ψ, Δ) are the traditional ellipsometric angles, and $N = \cos(2\psi)$ [not to be confused with the complex refractive index of (8.1)], $S = \sin(2\psi)\sin(\Delta)$, and $C = \sin(2\psi)\cos(\Delta)$ are elements of the sample Mueller matrix with the requirement that $N^2 + S^2 + C^2 = 1$. Figure 8.1 shows representative spectroscopic ellipsometry data for silicon with only the native oxide overlayer, expressed in terms of ρ and (ψ, Δ).

The quantity ρ can be converted directly into the pseudo-dielectric function

$$\langle\varepsilon\rangle = \langle\varepsilon_1\rangle - i\langle\varepsilon_2\rangle = \sin(\theta)^2\left[1 + \tan(\theta)^2\left(\frac{1-\rho}{1+\rho}\right)^2\right], \tag{8.6}$$

where θ is the angle of incidence. If there is no surface overlayer, then the pseudo-dielectric function becomes the actual dielectric function. Unfortunately, this is seldom the case. For silicon, there always is an overlayer consisting of oxides of silicon, hydrogen termination, surface roughness, etc., depending upon surface treatment. Even an overlayer of a few tenths of a nanometer can significantly distort the pseudodielectric function from the actual dielectric function.

8.2.2 Optical Functions of Silicon

In the spectral range $\lambda = 200–1200$ nm, the most reliable optical functions of silicon are determined from spectroscopic ellipsometry measurements in conjunction with optical transmission measurements. Spectroscopic ellipsometry measurements (described in Sect. 8.4) have been performed on a single crystal wafer of silicon, and the results are shown in Fig. 8.1. The dielectric functions and complex refractive indices are determined from the ellipsometry data using a procedure outlined in [12], where the surface overlayer was assumed to be a-SiO_2 using the refractive indices of Malitson [13]. The resulting values of n and k are shown in Fig. 8.2, along with an estimate of the errors.

As can be seen from Fig. 8.1, the value of Δ is close to 180° for wavelengths longer than ~500 nm, so it is important that the ellipsometric technique measure Mueller matrix elements proportional to sin(Δ) very accurately. This was very difficult using the older rotating polarizer or analyzer ellipsometers, since they did not contain a compensating element. This limitation does not exist with most modern ellipsometers based on rotating compensators or photoelastic modulators.

The optical functions of silicon have been the subject of many studies over the last 35 years, where the values that have been honed to such an extent that the disagreements are minimal [14–19]. For photon energies above the direct band gap (~3.4 eV or 365 nm), ellipsometry has been the experimental technique of choice,

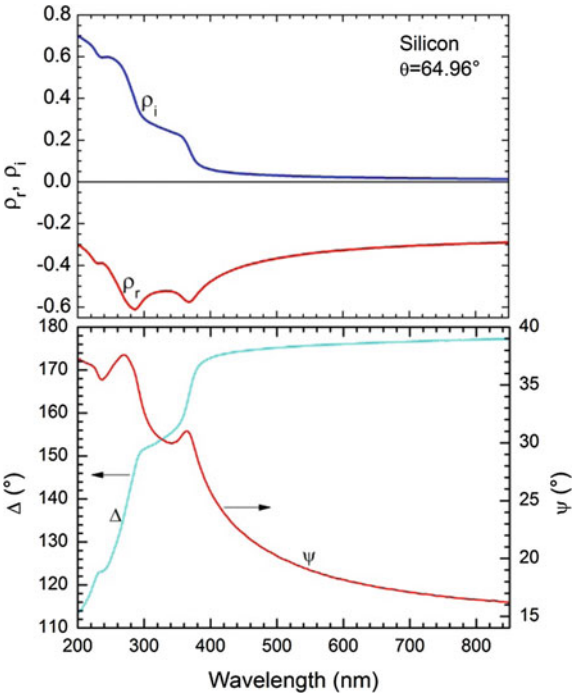

Fig. 8.1 Spectroscopic ellipsometry data for crystalline silicon with a native oxide layer, taken at an angle of incidence of 64.96°. The top panel expresses the data in terms of ρ_r and ρ_i and the bottom panel in terms of ψ and Δ

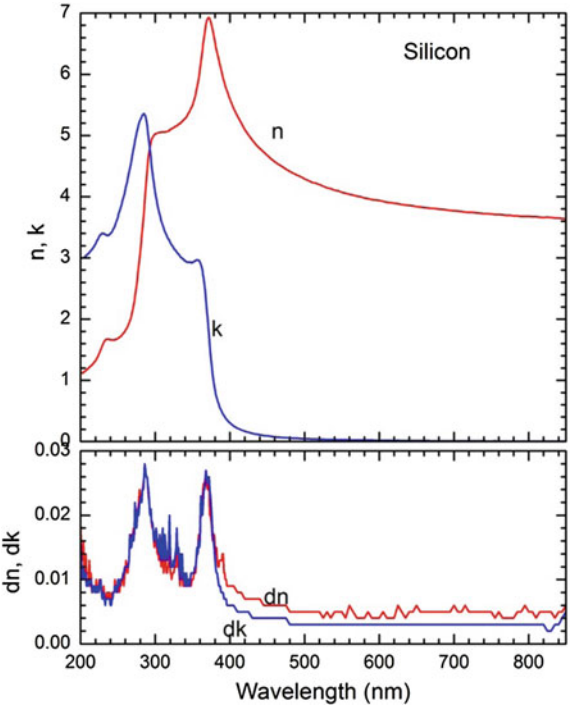

Fig. 8.2 The refractive index n and extinction coefficient k determined from the spectroscopic ellipsometry data shown in Fig. 8.1

although many different varieties of ellipsometers have been used. Interestingly, three of the most important considerations are sample preparation, surface orientation, and data analysis. The surface treatment (such as using an HF etch to clean the surface prior to measurement, or just using a sample with a stabilized native oxide) has a small but quite measurable effect on the data, as does the crystallographic orientation of the surface studied. If the surface layer is not entirely removed, it must be removed mathematically [15–17] to get the actual dielectric functions of silicon from the ellipsometry data, and that requires an appropriate model which will depend on the technique used to clean the silicon surface prior to measurement.

As might be expected, the primary disagreements between the data sets are small (~1–2%) and are focused near the critical points (290 and 370 nm) where the optical penetration depth is small, increasing the importance of the surface overlayer. For photon energies less than the direct band gap, a combination of spectroscopic ellipsometry and transmission measurements produce the most reliable values of the optical functions of silicon. Ellipsometry measurements produce reliable values of the refractive index (or ε_1) throughout the wavelength range, but produce increasingly inaccurate values of the extinction coefficient (or ε_2) as it becomes small. This is discussed in more detail in Sect. 8.4.

Using (8.2) and (8.3), the measured values of n and k can be transformed into reflectivity and absorption coefficient, as shown in Fig. 8.3. As can be seen from the

error bars on the ellipsometric determination of the absorption coefficient, this quantity becomes increasingly less accurate as k and α become smaller. For wavelengths longer than ~700 nm, transmission measurements become much more accurate than ellipsometric measurements in the determination of α or k and should be used instead of ellipsometric measurements. The transmission measurements show two interesting characteristics: First of all, there is a well-defined feature in the absorption coefficient curve at ~1050 nm. This is due to the optical absorption process for indirect gap semiconductors, which involve both the emission and absorption of a phonon; this was first discussed by Macfarlane et al. [5], and will be discussed later. Secondly, the transmission measurements show that the minimum photon energy for absorption in silicon at room temperature is ~1180 nm (=1.051 eV). This energy is somewhat less than the fundamental band gap, since a phonon can be absorbed to make up the energy difference.

In addition to the actual measurements of the dielectric functions of silicon, there have been several papers that have compiled the data [20–23], attempting to reconcile the small differences between the published data sets. Geist et al. [20, 21] fit the available room-temperature data resulting in a multi-parameter fit for both the refractive index and extinction coefficient from 3.1 to 1.1 eV (400–1127 nm). Green's compilation [23] tabulated data from 250 to 1450 nm and included an estimate of temperature coefficients.

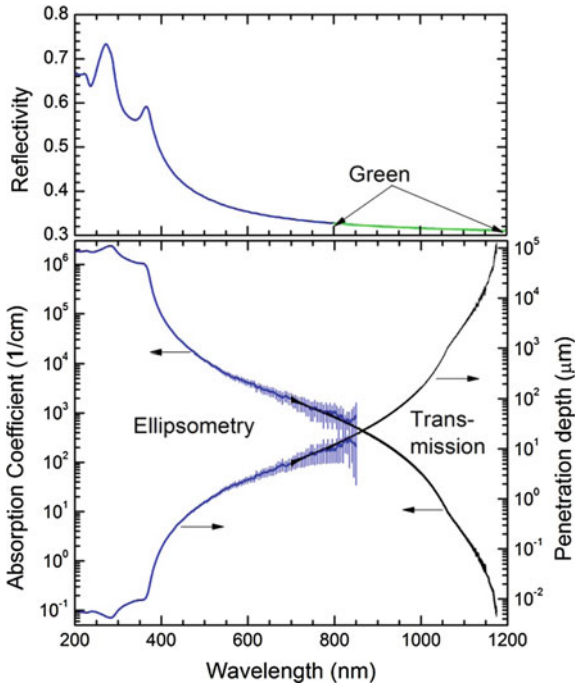

Fig. 8.3 The reflectivity (R, top) and optical absorption coefficient (α, bottom) for silicon. Ellipsometry measurements are shown from 200 to 850 nm for R and α, as well as the error limits for α. The compilation data from Green [22] is shown for R from 800 to 1200. Independent transmission data is shown for the absorption coefficient from 700 to 1200 nm. The equivalent penetration depth (in μm) is also shown in the bottom panel

8.2.3 Origins of the Optical Functions of Silicon

8.2.3.1 Band Structure and Critical Points

Many of the features observed in the refractive index and extinction coefficient of silicon (Fig. 8.2) below 400 nm are a result of direct optical transitions in crystalline silicon and can be understood from band structure. The details of band structure calculations are discussed in Chap. 4 (see also [24]). Briefly, the band structure of a material is a theoretical construct that calculates the energy levels that a single electron can have, given its wavevector **k**. The band structure will have the same symmetry that the crystal has, thus simplifying the calculation. As a result, points in the Brillouin zone can be labeled according to the symmetry of the crystal.

Figure 8.4 shows the dielectric function of silicon, plotted as a function of energy; this is the same data as presented in Fig. 8.2, using (8.1) to convert N to ε. The calculated band structure of silicon [25] is shown to the right of Fig. 8.4, which is plotted in two symmetry directions. The Γ point occurs for the wavevector $\mathbf{k} = (0, 0, 0)$ and is the center of Brillouin zone, while the L and X points represent the wavevector $\mathbf{k} = (\pi/a) * (1, 1, 1)$ and $= (\pi/a) * (1, 0, 0)$, respectively, where a is the dimension of the unit cell. The intermediate points are notated as Λ and Δ (not to be confused with the ellipsometric parameter Δ). The valence bands are represented by the electronic states less than 0 while the conduction bands all have energies greater than 0.

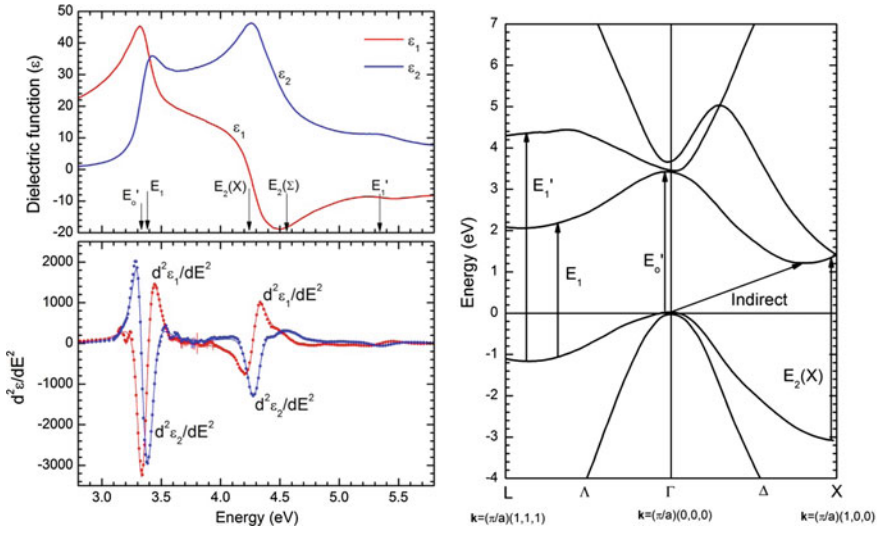

Fig. 8.4 Complex dielectric function of silicon as a function of energy and the 2nd derivative of the dielectric function with respect to energy (left). The energy positions of the 5 critical points are noted. The band structure of silicon [25] with the optical transitions noted (right)

Optical transitions in crystals can occur when a photon of a particular energy interacts with an electron in a filled state which is then excited to an unfilled state. For this discussion, the filled states will be in the valence band and the empty states in the conduction band. A direct transition occurs when there is no change in the wavevector **k** (vertical on the band structure diagram) and an indirect transition occurs when a change in the wavevector **k** is required. To conserve momentum, the indirect transition requires either the absorption or emission of a phonon (quantum of lattice vibration). The probability of transition depends on many things, including the probability that the valence band state is occupied and the conduction band state is unoccupied, the matrix element connecting the two states, and, for indirect transitions, the probability that a phonon of a particular **k**-vector exists or can be created. Since the indirect transition requires a phonon while a direct transition does not, generally direct transitions have a much higher transition probability, resulting in a much higher absorption coefficient. For direct transitions, the imaginary part of the dielectric function is given by [24]

$$\varepsilon_2\left(E_{\text{photon}}\right) \propto \sum_{\vec{k}} \left|P_{cv}\left(\vec{k}\right)\right|^2 \delta\left[E_c\left(\vec{k}\right) - E_v\left(\vec{k}\right) - E_{\text{photon}}\right] \propto \left|P_{cv}\right|^2 J_{cv}\left(E_{\text{photon}}\right) \quad (8.7)$$

where $P_{cv}(\mathbf{k})$ is the probability of transition (related to the symmetry of the critical point) and J_{cv} is the joint density of states.

In some cases, the energy positions of critical points in a crystal can be determined from the dielectric function spectra by taking the 2nd derivative of ε with respect to energy [25] (see Chap. 4),

$$\frac{\mathrm{d}^2\varepsilon(E)}{\mathrm{d}E^2} \approx Ae^{i\Phi}\left(E - E_{\mathrm{o}} + i\,\Gamma\right)^{n-2} = Fe^{i\Phi}\left(\varsigma + i\right)^{n-2}. \quad (8.8)$$

In (8.8), A is the amplitude of the transition, Φ is the phase, E_{o} is the threshold energy, and Γ is the broadening. The exponent n depends on the dimensionality of the critical point ($n = -1/2$ (1-D), 0 (2-D), ½ (3-D), −1 (discrete exciton)). The second expression in (8.8) represents a re-parameterization that eliminates some correlations, where $F = A/\Gamma^{n-2}$ and $\zeta = (E - E_{\mathrm{o}})/\Gamma$.

The bottom left of Fig. 8.4 shows the 2nd derivative of ε with respect to energy for silicon at 295 K, along with a fit to the data using 5 critical points. The energies of these critical points are shown in Table 8.1, along with the energies determined by Lautenschlager et al. [25], and can then be related to critical points in the Brillouin zone of silicon, as plotted on the band structure diagram of silicon to the right of Fig. 8.4. The lowest energy direct transition (E_{o}') occurs at the Γ point and is often called the direct transition edge. This transition is accompanied by another direct transition (E_1) near the L-point. The largest value of ε_2 occurs near 4.25 eV and is represented by the critical points at $E_2(X)$ and $E_2(\Sigma)$. The E_1' transition occurs near the L point and is quite weak.

Table 8.1 Critical point energies as determined by taking 2nd derivatives of the dielectric function as a function of energy and fitting to (8.8)

	Lautenschager et al. [24]	This work
E_o'	3.320 ± 0.005	3.327 ± 0.002
E_1	3.396 ± 0.005	3.382 ± 0.005
$E_2(X)$	4.270 ± 0.002	4.283 ± 0.003
$E_2(\Sigma)$	4.492 ± 0.010	4.551 ± 0.021
E_1'	5.317 ± 0.025	5.346 ± 0.023

8.2.3.2 Indirect Absorption

Over most of the solar spectrum, optical absorption in silicon is indirect and requires a phonon to conserve the wavevector **k**. The phonon can be either emitted (Stokes) or absorbed (anti-Stokes). For the case of silicon, there are two primary phonons involved: the transverse acoustic and the longitudinal acoustic. Therefore, there are 4 primary contributions to the absorption coefficient near the band edge. These absorption coefficients will be functions of both the photon energy and the temperature of the material and can be expressed as:

$$\alpha(E,T) = \alpha_{LS}(E,T) + \alpha_{LaS}(E,T) + \alpha_{TS}(E,T) + \alpha_{TaS}(E,T), \tag{8.9}$$

where the subscripts indicate either the longitudinal (L) or the transverse (T) acoustic phonon, and phonon emission (Stokes, S) or phonon absorption (anti-Stokes aS).

The phonon absorption process is proportional to the probability that a phonon state is occupied for the absorption process (anti-Stokes), which is given by Bose-Einstein statistics:

$$f_{BE}(T,\theta) = \frac{1}{\left(\exp\left(\frac{\theta}{k_B T}\right) - 1\right)} \tag{8.10a}$$

where T is the temperature in Kelvin, θ is the energy of the phonon in eV, and k_B is Boltzmann's constant = 8.617×10^{-5} eV/K. Conversely, the phonon emission process requires that the phonon state be empty, which is $[1 - f_{BE}(\theta,T)]$. The other factors involved in the determination of optical absorption are the joint density of states and the matrix element which connects an occupied state in the valence band with an unoccupied state in the conduction band.

Figure 8.5 shows the absorption coefficient data for silicon near the band edge, along with a fit to the data using the expressions:

$$\alpha_{LS}(E,T) = (1 - f_{BE}(\theta_L,T))\left(A_L\sqrt{E_{LS}} + B_L(E_{LS})^{\beta}\right) \quad E_{LS} = E - E_g(T) - \theta_L \tag{8.10b}$$

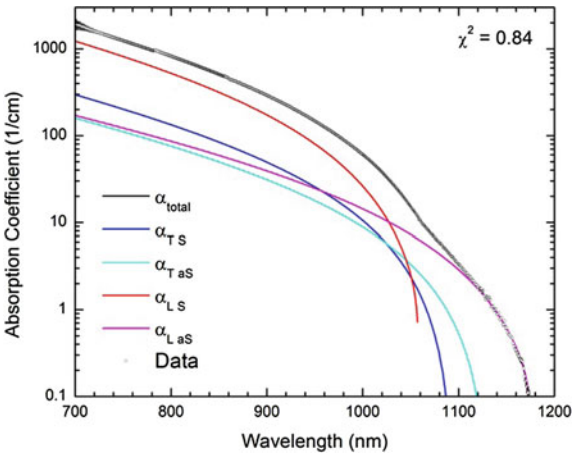

Fig. 8.5 Absorption Coefficient of silicon data (black) compared with calculated absorption coefficients described in the text. The 4 partial absorption coefficients are indicated by the subscripts L and T for the longitudinal and transverse acoustic phonons and S and aS for the Stokes (emission) and anti-Stokes (absorption) processes

$$\alpha_{\mathrm{LaS}}(E,T) = f_{\mathrm{BE}}(\theta_{\mathrm{L}},T)\left(A_{\mathrm{L}}\sqrt{E_{\mathrm{LaS}}} + B_{\mathrm{L}}(E_{\mathrm{LaS}})^{\beta}\right) \quad E_{\mathrm{LaS}} = E - E_{\mathrm{g}}(T) + \theta_{\mathrm{L}} \tag{8.10c}$$

$$\alpha_{\mathrm{TS}}(E,T) = (1 - f_{\mathrm{BE}}(\theta_{\mathrm{T}},T))\left(B_{\mathrm{T}}(E_{\mathrm{TS}})^{\beta}\right) \quad E_{\mathrm{TS}} = E - E_{\mathrm{g}}(T) - \theta_{\mathrm{T}} \tag{8.10d}$$

$$\alpha_{\mathrm{TaS}}(E,T) = f_{\mathrm{BE}}(\theta_{\mathrm{T}},T)\left(B_{\mathrm{T}}(E_{\mathrm{TaS}})^{\beta}\right) \quad E_{\mathrm{TaS}} = E - E_{\mathrm{g}}(T) + \theta_{\mathrm{T}} \tag{8.10e}$$

The fitting parameters are A_{L}, B_{L}, θ_{L}, B_{T}, θ_{T}, E_{g}(T) and the exponent β. The fundamental indirect gap energy of silicon is given by $E_{\mathrm{g}}(T)$, where the temperature dependence is expressed explicitly. The phonon energies θ_{L} and θ_{T} are given in eV. This formulation is very similar to that given in [5], with the exception that their β function is replaced with the exponent β, which is treated as a fitting parameter. For parabolic bands with a constant transition matrix element, $\beta = 2$.

The fitted parameters of (8.9) and (8.10a–8.10e) have been determined by minimizing the reduced χ^2 using the Levenberg-Marquardt algorithm resulting in the values given in Table 8.2. Seven (7) parameters were fit, including fundamental band gap. As can be seen the fit is excellent with a reduced $\chi^2 = 0.84$, indicating that the model fits the data.

Table 8.2 Fitted parameters to the data shown in Fig. 8.5. The sample temperature was 295 K

A_{L}	19.85 ± 0.38	1/cm
B_{L}	2846 ± 22	1/cm
θ_{L}	0.0585 ± 0.0001	eV
B_{T}	355 ± 25	1/cm
θ_{T}	0.0185 ± 0.0010	eV
β	1.874 ± 0.003	
$E_{\mathrm{g}}(T)$	1.1134 ± 0.0002	eV

The values given in Table 8.2 are somewhat different from those used in [5, 11], but this is to be expected since the measured absorption coefficients in this work were considerably larger than those measured in [5] (<~2000 cm^{-1} compared to <~40 cm^{-1}) and the wavelengths examined in this work are quite different from that of [11] (700–1200 nm compared to a single wavelength 1152 nm). Clearly, the dominant phonon in the indirect optical absorption is the longitudinal acoustic phonon, and both the emission (Stokes) and absorption (anti-Stokes) processes are important, depending on the wavelength. The kink in the absorption coefficient curve is real and the result of both the emission and absorption of a phonon playing a role in the total absorption coefficient. The deviation of the exponent β from 2 is an indication that the valence and conduction bands are no longer parabolic when photon energies much larger than the fundamental band gap are considered. Temperature also plays a significant role as discussed in the next section.

8.2.4 *Modifications to the Optical Properties of Silicon*

While the optical properties are often labeled as optical constants, this is actually a misnomer, since they are anything but constant. Obviously, the optical properties depend significantly on wavelength, as has been discussed in the previous section. However, several other factors can also affect the optical properties, including temperature, morphology, doping, and stress. Of these modifications, temperature and morphology are the most important to photovoltaics. Spectroscopic ellipsometry measurements, along with transmission measurements where appropriate, have been used to quantify the dependence of the optical properties of silicon on these perturbations.

It has been known for some time that the optical functions of silicon depend significantly on temperature [5, 10, 11, 25–30]. Figure 8.6 shows the changes in the optical functions of silicon with increasing temperature [30]. The critical points broaden and increase in wavelength (see Lautenschlager [25] for a complete description). From the thermodynamic arguments of Thurmond, the fundamental indirect gap energy is given by [26]

$$E_g(T) = 1.155 - \frac{4.73 \cdot 10^{-4} T^2}{635 + T}, \tag{8.11}$$

where the temperature T is expressed in Kelvin. At room temperature (295 K), $E_g = 1.1107$, which compares to the fitted value of 1.1134 eV, given in Table 8.2.

Figure 8.7 shows the temperature dependence of the absorption coefficient, plotted semilogarithmically, with the temperature-dependent fundamental band gap from (8.11) shown in the insert. The short wavelength region (<850 nm) is taken from the data shown in Fig. 6 [30], while the long wavelength region (>700 nm) is determined from (8.9) and (8.10a–8.10e) and is labeled "Transmission." Clearly, the transmission and ellipsometry values of the absorption coefficient agree within

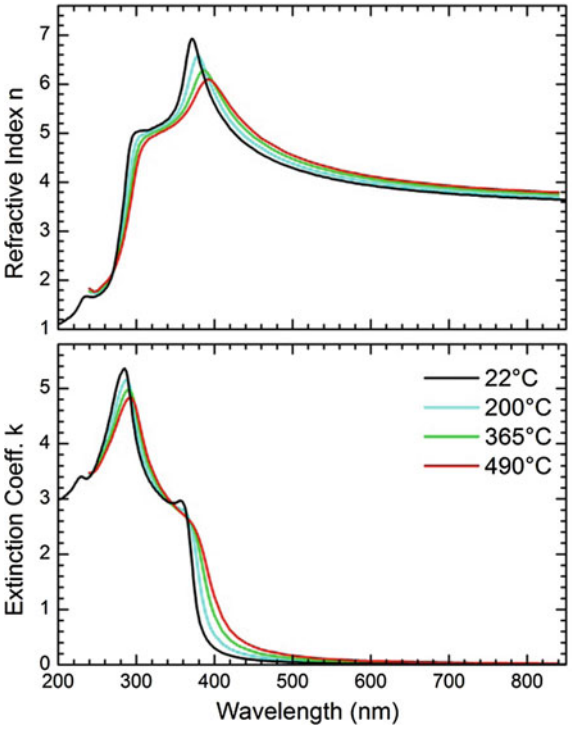

Fig. 8.6 The refractive index and extinction coefficient of silicon as a function of temperature, determined by spectroscopic ellipsometry [30]

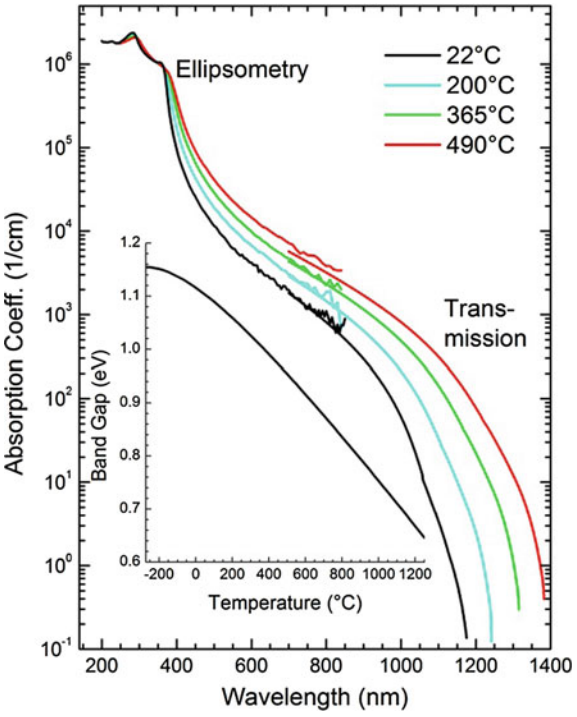

Fig. 8.7 The absorption coefficient of silicon as a function of temperature. The short wavelength region (<850 nm) was determined using spectroscopic ellipsometry data [30], while the long wavelength data (700–1400 nm) was calculated using (8.9) and (8.10a–8.10e). The inset shows the fundamental band gap energy of silicon as a function of temperature, calculated using (8.11)

error for the 22, 200 and 365 °C spectra, while the ellipsometry value of the absorption coefficient is a little larger than the transmission values for the 490 °C sample. This is likely due to an under-estimate of the overlayer thickness used in reducing the ellipsometry data to n and k.

In the region of primary interest to photovoltaics (below the direct band edge or for wavelengths greater than 400 nm), it can be seen that the refractive index, extinction coefficient and absorption coefficient all increase with temperature. The refractive index increase is small, well-ordered, and shows dispersive behavior, being larger for smaller wavelengths. The extinction coefficient and absorption coefficient are far more complicated, and increase dramatically with temperature over the entire wavelength range 400–1200 nm. In the region from 400 to 700 nm, early ellipsometry results [27, 28] showed that the absorption coefficient depended exponentially on temperature, which is validated here. Near the indirect band edge (900–1400 nm), the behavior is even more complicated due to the decrease in the fundamental band gap with temperature and the importance of the temperature dependence on the phonon population. Specifically, the anti-Stokes process, which requires the absorption of a phonon, will become more important at higher temperatures, since there are more phonons available. As Macfarlane et al. [5] showed, reducing the temperature well below room temperature significantly reduces the availability of phonons, thus reducing the anti-Stokes process. This is all accounted for in (8.9) and (8.10a–8.10e).

In the wavelength region of 400–850 nm, the data shown in Fig. 8.6 has been parameterized, using 5 parameters for the refractive index and 6 parameters for the extinction coefficient [30]. The resulting expressions are given by:

$$n(E,T) = n_o + a(E)T \tag{8.12a}$$

$$n_o(E) = \sqrt{4.565 + \frac{97.3}{E_{dg}^2 - E^2}} \tag{8.12b}$$

$$a(E) = 10^{-4}\left(-1.864 + \frac{53.94}{E_{dg}^2 - E^2}\right) \tag{8.12c}$$

$$k(E,T) = k_o(E)\exp\left(\frac{T}{T_o(E)}\right) \tag{8.13a}$$

$$k_o(E) = -0.0805 + \exp\left(-3.1893 + \frac{7.946}{E_{dg}^2 - E^2}\right) \tag{8.13b}$$

$$T_o(E) = 369.9 - \exp(-12.92 + 5.509E) \tag{8.13c}$$

where the parameter $E_{dg} = 3.648$ eV and is common to both n and k. It is important to understand that these expressions are only valid for wavelengths longer than the

direct band edge in silicon, which will increase with increasing temperature. At room temperature, these expressions are valid from 375 to 850 nm, and at 500 °C, the expressions are valid from 410 to 850 nm.

Near room temperature, the change in refractive index and absorption coefficient can be calculated using the expressions given in (8.9)–(8.13a–8.13c), and are shown in Fig. 8.8, where $(1/n)\ dn/dT$ and $(1/\alpha)\ d\alpha/dT$ are plotted. The temperature coefficient of the refractive index is shown in the top panel of Fig. 8.8, and shows typical dispersive behavior, where the coefficient decreases at longer wavelengths. The bottom panel in Fig. 8.8 shows the temperature coefficient for the absorption coefficient plotted semilogarithmically. Below 700 nm, the derivatives were determined numerically from (8.13a–8.13c), while above 700 nm, the derivatives were determined from (8.9) and (8.10a–8.10e). The nearly constant temperature coefficient of the absorption coefficient observed from 450 to 750 nm is consistent with the observed exponential behavior of the absorption coefficient from early ellipsometry experiments [27]. The expression for the temperature coefficient of α is decidedly non-linear near the band edge, since the fundamental band gap is shifting to lower energies with increasing temperature and the population of phonons is increasing with increasing temperature. Therefore, the data presented in Fig. 8.8 is only valid near room temperature. However, one might use the expressions presented in (8.9) and (8.10a–8.10e) to calculate the temperature coefficient at other temperatures.

The optical functions of silicon are also dependent on the doping concentrations, as seen in Fig. 8.9. These samples were prepared by ion implantation followed by laser annealing [31], which results in higher doping densities than are attainable using traditional dopant activation techniques. The optical effects are similar for other n-type dopants such as phosphorus or antimony, but significantly less for p-type dopants such as boron. With very high doping densities, the critical points are broadened, and significant changes occur below the direct band gap. This effect is usually of no concern for photovoltaic applications, since conventional

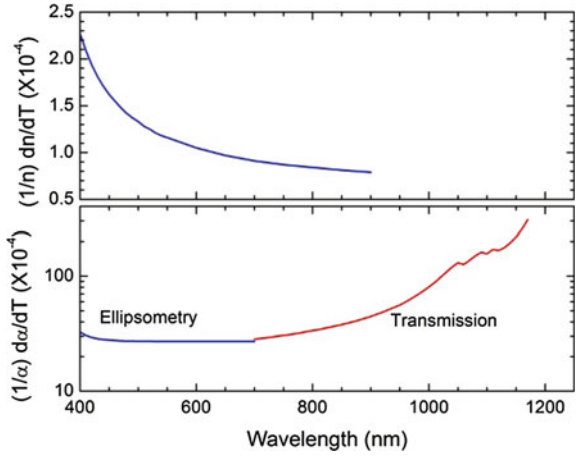

Fig. 8.8 The temperature coefficients of the refractive index and absorption coefficient determined from (8.9), (8.10a–8.10e), (8.12a–8.12c) and (8.13a–8.13c)

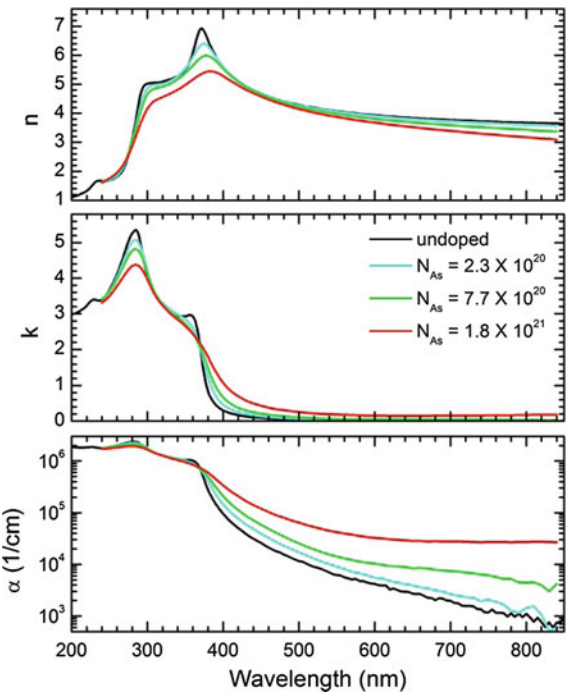

Fig. 8.9 Spectroscopic ellipsometry measurements of the refractive index, extinction coefficient, and absorption coefficient for silicon as a function of doping level (from [31])

photovoltaic doping densities are much lower than is required to see a change in the optical functions.

As might be expected, the optical functions of silicon are also dependent upon the morphology of the material, shown in Fig. 8.10 [32]. The optical functions of semicrystalline silicon (typical grain size of ~0.1–1 mm) show nearly the same optical functions as crystalline silicon, but polycrystalline silicon shows quite different values of the optical functions. Large grain polycrystalline silicon (p-Si LG, grain size ~250 nm) shows optical functions very similar to crystalline silicon, but with broadened critical points and increased absorption below the direct band edge. Small grain polycrystalline silicon (p-Si SG, grain size ~10–20 nm) shows optical functions that are even more broadened, but still resemble the optical functions of crystalline silicon. Amorphous silicon shows significantly different values in the optical functions, and loses any semblance of critical points which are still observable in large-grain and small-grain polycrystalline silicon.

If silicon is strained [33, 34], then the material is no longer strictly cubic, but must be treated as an anisotropic material. The effects on the optical properties near the critical points have been studied by Etchegoin et al. [33], where strains in excess of 0.1 GPa will shift critical points sufficiently to be observed. Similarly, the indirect gap energy will be affected by similar strains [34]. Since the required strains are so large to generate differences in the optical spectra, these effects can normally be ignored in photovoltaics.

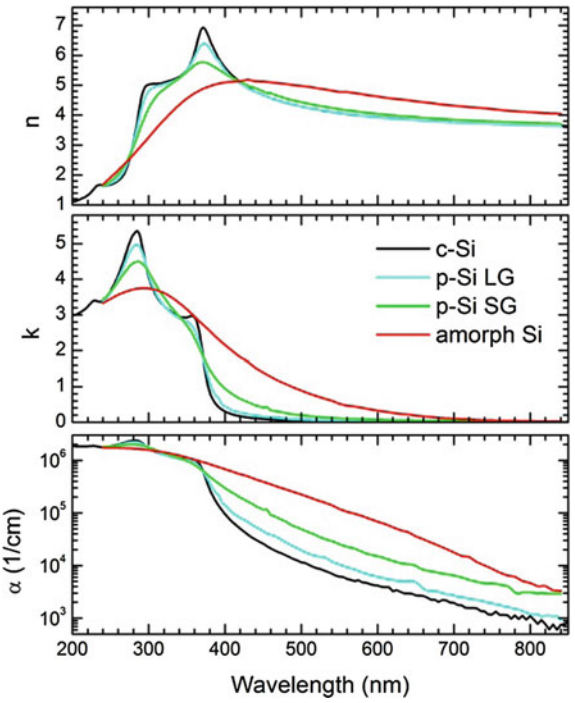

Fig. 8.10 Spectroscopic ellipsometry measurements of the refractive index, extinction coefficient, and absorption coefficient for various morphologies of silicon (from [32])

Silicon melts at 1414 °C, where it becomes metallic. Therefore, its optical properties are considerably different from the solid. Moreover, liquid silicon is very reactive in air, so performing optical measurements on a liquid pool would mean that a significant overlayer would form, which would have to be taken into account in the data analysis. To avoid this complication, measurements of the optical functions of liquid silicon were performed at several cw laser wavelengths using

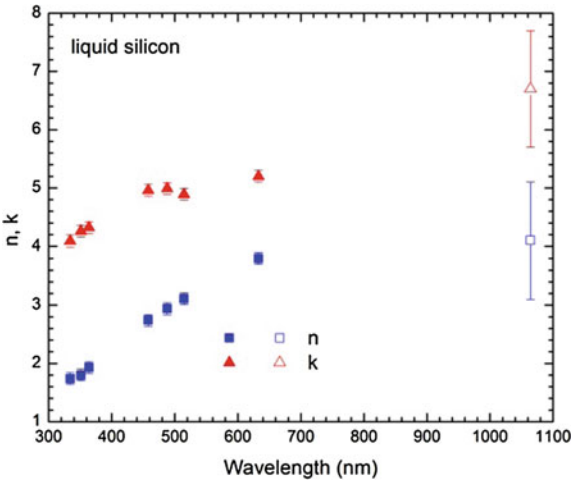

Fig. 8.11 Refractive index n and extinction coefficient of liquid silicon. The solid data points were obtained from [35, 36] where an excimer laser was used to liquefy the silicon surface for ~100 ns. The open points were obtained from [37]

time-resolved ellipsometry [35, 36] during a laser annealing experiment, where the sample surface remains molten for ~100 ns. Similar measurements were done at 1065 nm by Li and Fauchet [37], where the reflectivity was monitored. These results are shown in Fig. 8.11.

8.3 Spectroscopic Ellipsometry of Thin Films on Silicon

There are several dielectric and semiconductor thin films that are commonly used in the silicon photovoltaics industry that are routinely characterized using spectroscopic ellipsometry. As has been shown in Sect. 8.2.4, the optical properties of silicon are dependent on several factors, only one of which is the wavelength of light. This is also true for thin films. Obviously, the optical properties will depend on wavelength and on the constituents of the film. Not so obviously, the optical properties can also depend upon morphology, deposition technique, thickness, impurity type and concentration, etc. Since spectroscopic ellipsometry is non-destructive and is very sensitive to thickness, refractive index, and extinction coefficient, it often is the ideal technique to monitor thin film quality.

Since the optical functions of thin films can vary considerably with deposition conditions, it is important to be able to parameterize these optical functions to analyze spectroscopic ellipsometry measurements. If the material has a band gap that is considerably larger than the highest measured energy, then it is usually a good approximation to model the optical functions of the film using either the Sellmeier equation or the Cauchy expression (discussed in Chap. 5). The Sellmeier approximation is based on the Lorentz oscillator model, where it is assumed that the absorptive part is zero. This expression is given by

$$\varepsilon(\lambda) = n^2(\lambda) = \varepsilon_\infty + \frac{A\lambda^2}{\lambda^2 - \lambda_o^2}, \tag{8.14a}$$

where λ_o is the resonance wavelength of the oscillator (assumed to be less than the smallest measured wavelength), A is the amplitude of the oscillator, and ε_∞ is the dielectric constant at large energy or very small wavelength (this is often 1). If it can be assumed that $\varepsilon_\infty = 1$, then the Sellmeier approximation requires only two fitting parameters A and λ_o. The Sellmeier approximation is often a good model for SiO_2 films on silicon, where $A = 1.099$ and $\lambda_o = 93$ nm.

The Cauchy formula is an empirical relationship that is given by

$$n(\lambda) = A + \frac{B}{\lambda^2} + \frac{C}{\lambda^4} + \cdots, \tag{8.14b}$$

where it is assumed that the absorptive part is zero. Often, the first two parameters are sufficient to fit the spectroscopic variation of the refractive index. For fused silica in the visible range (400–700 nm), $A = 1.458$, $B = 0.00354$ and $C = 0$.

Generally, the Sellmeier expression (8.14a) is more accurate, particularly if the wavelength range of interest extends into the ultraviolet.

If the band gap of the film falls within the wavelength range of the spectroscopic ellipsometry measurement, then the Sellmeier or Cauchy approximations will not be appropriate and a more sophisticated model must be employed. In this case, the extinction coefficient (or the imaginary part of the dielectric function) will be non-zero and needs to be modeled as well as the refractive index. One such model that works quite well for amorphous thin films is the Tauc-Lorentz model [38], which is based on the Tauc band edge [39] convoluted with a Lorentz oscillator to approximate the joint density of states and optical transition probabilities. The imaginary part of the complex dielectric function of the Tauc-Lorentz model is given by

$$\varepsilon_2(E) = 2n(E)k(E) = \frac{A\left(E - E_g\right)^2}{E\left[\left(E^2 - E_o^2\right)^2 + C^2E^2\right]}\Theta\left(E - E_g\right) \tag{8.15a}$$

The real part is determined by performing the Kramers-Kronig integral of $\varepsilon_2(E)$:

$$\varepsilon_1(E) = n^2(E) - k^2(E) = \varepsilon_1(\infty) + \frac{2}{\pi}P\int_{E_g}^{\infty}\frac{\xi\varepsilon_2(E)}{\xi^2 - E^2}\mathrm{d}\xi \tag{8.15b}$$

In (8.15a, 8.15b), E_g is the band gap of the amorphous semiconductor, E_o is the maximum energy of the Lorentz oscillator, C is the broadening parameter, and A is the amplitude. As with the Sellmeier approximation, $\varepsilon_1(\infty)$ is often 1, but can be greater than 1 if there are significant optical transitions at energies greater than sampled by the ellipsometer. The Kramers-Kronig integral can be evaluated exactly, but is too long to be presented here (see [38]). Please note that the amplitude A given here is somewhat different from the expression given in [38], where $A_{new} = A_{old}E_oC$.

Another approach to the modeling of the optical properties of amorphous materials was presented by Ferlauto et al. [40] where Urbach tail absorption is included and the formulation of ε_2 is based on the Cody assumption (parabolic bands and constant dipole matrix element) [41] rather than the Tauc assumption (parabolic bands and constant momentum matrix element). This formulation has a decided advantage of the Tauc-Lorentz formulation when optical transmission studies are included in the data analysis, but the Cody-Lorentz formulation does involve more fitting parameters. In many cases, the difference between the two models is marginal.

As an example of spectroscopic ellipsometry characterization of a thin film system, consider a film of amorphous silicon nitride doped with significant hydrogen (a-Si_xN_y:H) grown on a film of SiO_2 with a silicon substrate. The resulting spectroscopic ellipsometry data (taken from [42]) and the resulting fit are shown in Fig. 8.12. The model used is shown graphically in Fig. 8.12 and consisted of a rough layer, a layer of amorphous non-stoichiometric, hydrogen incorporated

silicon nitride (a-Si_xN_y:H), a layer of silicon dioxide(a-SiO_2), and a substrate of crystalline silicon (c-Si). The rough layer was modeled using the Bruggeman effective medium approximation (see Chap. 3), the silicon nitride layer was modeled by the Tauc-Lorentz formulation [see (8.15a, 8.15b)], and the silicon dioxide layer was modeled by the Sellmeier approximation [see (8.14a)]. The results of the fits are detailed in Table 8.3. Fit 1 utilized 9 fitting parameters, and resulted in significant correlations between the two a-SiO_2 fitting parameters and other parameters in the model. Since the a-SiO_2 parameters are close to those expected for a-SiO_2, a second fit was attempted, where the values of the two a-SiO_2 parameters where held constant at the a-SiO_2 values. As can be seen from Table 8.3, the resulting χ^2 is only marginally higher than that for fit 1, yet the correlated errors for the SiO_2 thickness and some of the Tauc-Lorentz parameters have decreased significantly. The resulting values of the refractive index and extinction coefficient of the a-Si_xN_y:H film are shown in Fig. 8.13, labeled with the energy gap $E_g = 3.82$ eV.

Figure 8.13 shows the refractive index and extinction coefficient for several silicon nitride films determined using spectroscopic ellipsometry measurements analyzed using the Tauc-Lorentz model [43, 44]. The films were grown using plasma-enhanced chemical vapor deposition (PECVD), where the various optical properties are obtained by varying the growth and post-growth conditions. The resulting amorphous film composition is non-stoichiometric silicon nitride with some hydrogen incorporation. As can be seen from Fig. 8.13, the various growth conditions result in quite different optical properties. Generally speaking, the refractive index is controlled by controlling the silane to ammonia flow rate. If the silicon to nitrogen ratio is close to 3–4, then the refractive index tends to be low (~2.02 at 600 nm) with a high-energy band gap. If there is considerably more silicon, then the refractive index tends to be higher, but the band gap tends to be lower. Depending on deposition conditions, there can be significant hydrogen and

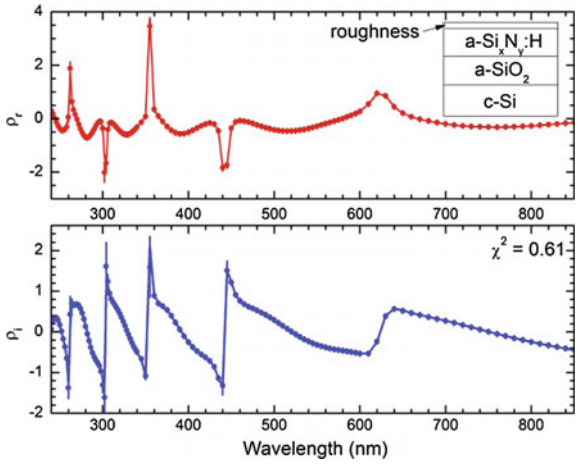

Fig. 8.12 Real and imaginary parts of ρ from a spectroscopic ellipsometry measurement on a-Si_xN_y:H on SiO_2 on c-Si film [42]. The fit line is shown as are the errors. Table 8.3 shows the fitting results

Table 8.3 The fitting results from the spectroscopic ellipsometry data shown in Fig. 8.12. Fit 1 optimized 9 parameters while Fit 2 optimized only 7 parameters, where the Sellmeier coefficients for the SiO_2 layer (indicated with NF) were held constant. The errors shown are the correlated errors

Parameter	Fit 1 ($\chi^2 = 0.61$)	Fit 2 ($\chi^2 = 0.62$)
Rough thick (nm)	2.6 ± 0.3	2.6 ± 0.3
SiN thick (nm)	232.2 ± 0.6	232.4 ± 0.5
SiN TL A	4044 ± 455	4243 ± 380
SiN TL E_g (eV)	3.82 ± 0.03	3.82 ± 0.03
SiN TL E_0 (eV)	9.18 ± 0.09	9.24 ± 0.04
SiN TL C (eV)	4.14 ± 0.33	4.29 ± 0.27
SiO_2 Thick (nm)	294.7 ± 1.5	295.9 ± 0.2
SiO_2 Sel A	1.112 ± 0.014	1.099 (NF)
SiO_2 Sel λ_o (nm)	91.2 ± 2.4	93 (NF)

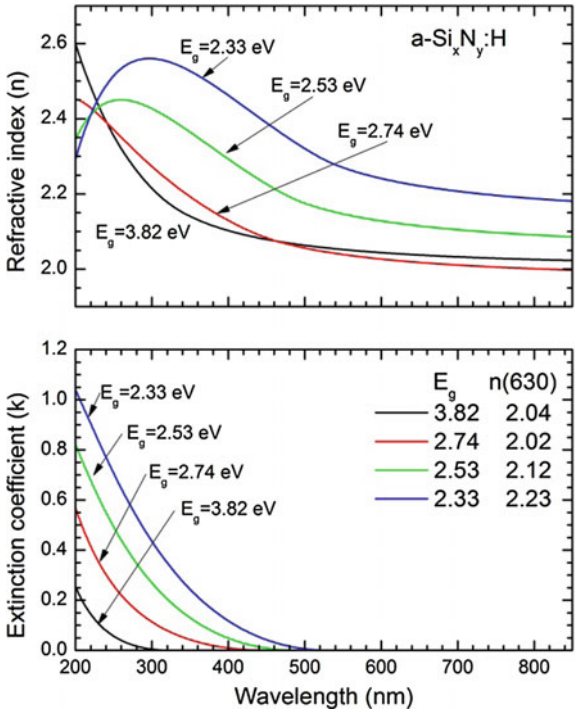

Fig. 8.13 The refractive index n and extinction coefficient k for several silicon nitride films measured using spectroscopic ellipsometry and analyzed using the Tauc-Lorentz model. The lines are labeled according to the resulting band gap (E_g) and the refractive index at 630 nm

void incorporation, which will also affect the refractive index and extinction coefficient. While a higher refractive index may be better for some applications, the lower band gap means that more of the ultraviolet light will be absorbed in the coating, and this trade-off must be taken into account in coating design.

Since silicon nitride can have such a wide range of optical properties, all controlled by the growth conditions, it makes an ideal material for anti-reflection coatings on silicon solar cells. Reference [44] describes an early study, where a variety of silicon nitride films were grown, measured using spectroscopic

ellipsometry, and then evaluated as potential anti-reflection coatings. Since the refractive index is a function of growth conditions, it is possible to deposit multiple layers of silicon nitride that will be more efficient as an antireflection coating than a single layer. Since the band gap of amorphous silicon nitride falls within the part of the spectrum of interest to photovoltaics, light absorption from the silicon nitride must be taken into account in the anti-reflection coating design.

Generally speaking, spectroscopic ellipsometry measurements are best carried out on smooth surfaces. Small amounts of surface roughness can be addressed using the Bruggeman effective medium approximation, as was done above for the data shown in Fig. 8.12. However, many high-efficiency silicon solar cells have a very rough surface that has been textured using a preferential etch. On single crystal silicon solar cells, this texturing results in the formation of pyramidal structures that are randomly positioned, but of the same orientation. The size of these pyramids is 2–8 μm, which is considerably greater than the wavelength of light used in ellipsometry experiments, resulting in significant light scatter. One solution to this is to tilt the sample in the ellipsometer to 54.7°, such that the ellipsometer light reflects off the sides of the pyramids [45]. This scheme has been used to characterize a-Si_xN_y:H films even on textured mono-crystalline silicon solar cells.

Thin films of amorphous silicon dioxide (a-SiO_2) are commonly found in any silicon technology, including solar cell manufacture. Left in air, silicon will naturally oxidize, stabilizing at a thickness of ~2 nm over several years. The most accurate values of the spectroscopic refractive index of bulk fused silica (a-SiO_2) were determined using the minimum deviation method [13]. The band edge of a-SiO_2 is ~9 eV (~140 nm), so the Sellmeier approximation (8.14a) is sufficient for most ellipsometric measurements. Relatively thick a-SiO_2 films (>100 nm) have spectroscopic refractive indices similar to fused silica, but may vary slightly with differing deposition conditions and water content. Some work has shown that the refractive index of very thin film a-SiO_2 is somewhat higher than bulk a-SiO_2 [46, 47], but others [48] disagree; this probably depends on deposition conditions. Note that the refractive index and thickness of a very thin film become more coupled as the film thickness decreases, making a separate measurement of film thickness and refractive index more difficult. Obviously, if a film growth technique is employed that results in non-stoichiometric a-SiO_x, then the optical functions will be considerably different from thin-film SiO_2 and the Tauc-Lorentz or Cody-Lorentz formulations will be the more appropriate model.

Another film of interest to photovoltaics is Al_2O_3, which can act as a surface passivation layer [49]. Near-stoichiometric Al_2O_3 films will have a refractive index $n \sim 1.60$–1.65 at 620 nm with no observable absorption in the wavelength range 190–1000 nm. This refractive index is considerably less than the refractive index of crystalline Al_2O_3 ($n(o) = 1.7675$, $n(e) = 1.7594$ at 620 nm [50]). As a result, the refractive index of Al_2O_3 films can also be monitored using either the Sellmeier or Cauchy expressions [(8.14a) and (8.14b)]. For solar cell passivation, typical thicknesses are thin (7–30 nm), making spectroscopic ellipsometry the ideal diagnostic for this application. In [49], these films were grown using plasma-assisted atomic layer deposition resulting in surface recombination velocities of 2–6 cm/s.

8.4 Addendum: Optical Data Tables

The spectroscopic ellipsometry room temperature optical data shown in Figs. 8.1, 8.2, 8.3, 8.4, 8.6, 8.7, 8.9, and 8.10 were taken using the two-modulator generalized ellipsometer (2-MGE) [51] on an n-type (100) silicon wafer where the oxide layer was stabilized for several years. The raw data is shown in Fig. 8.1, where the dielectric function and complex refractive index are determined by mathematically removing the surface overlayer using the Newton-Raphson algorithm described in [12], where the a-SiO_2 refractive index values of Malitson [13] were taken for the overlayer. The angle of incidence was $64.96 \pm 0.01°$ and the thickness of the overlayer was 2.19 ± 0.01 nm. Error limits were determined that included the stochastic errors, as well as the systematic errors of the angle of incidence, the overlayer thickness and accidental misalignment of the optics. Additional error, not included, arises from the model chosen to represent the optical functions of the overlayer. The thickness of the a-SiO_2 overlayer was chosen such that the value of k as measured by spectroscopic ellipsometry measurements matched up with the value of k determined from transmission measurements in the 700–800 nm range. If the error limits are taken into account, there is no significant difference between this data and the data presented in [15] although the instruments were quite different.

The absorption coefficients from 700 to 1200 nm shown in Figs. 8.3 and 8.5 were determined using optical transmission measurements of several samples of double-sided polished silicon wafers of various thicknesses from 40 to 240 μm. The transmission measurements were taken using a Perkin-Elmer Lambda 900 spectrophotometer, and the absorption coefficients were determined from the transmission measurements as described in Sect. 8.2. Errors were also determined from estimates of the spectrometer error and the error in the measurement of the thickness of the various wafers. These errors are most pronounced in the 700–800 nm range (see Fig. 8.5) where there is very little light transmission even through the thinnest silicon wafer.

The data shown in Part II Chapter 8.2.1 (Vol. 2) of this book is a compilation of this data. The refractive index data from 300 to 850 nm was taken from the 2-MGE measurements, and the refractive index from 850 to 1200 nm was taken from the work of Herzinger [17] and Green [23]. The 2-MGE data was used for the extinction coefficient from 300 to 700 nm. From 700 to 1200 nm, the calculated absorption coefficient (transformed to extinction coefficient) from (8.9) and (8.10a–8.10e) was used, where the coefficients of Table 8.2 were used. Recall that this expression was a fit to the experimental data and associated error with a reduced $\chi^2 = 0.84$. This data set agrees with the compilation of Geist [21] and the measurements of Schinke [18] within 1–2%, which is within the error of the measurement. However, this data set is ~5% less than the compilation of Green [22], which may be due to small differences in the actual sample temperature during measurement.

Table 8.4 shows a comparison between the various data sets obtained from ellipsometry measurements as well as the compilations of Geist [21] and Green [23]. Three wavelengths were chosen for comparison: 350 nm (just above the direct band

Table 8.4 Comparison of various data sets, including the average and an estimate of the standard deviation. The data used in this work is also shown, along with the error associated with each data point

Author	n(350)	n(400)	n(700)	k(350)	k(400)	k(700)
Aspnes (1983) [14]	5.484	5.587	3.772	2.904	0.298	0.011
Jellison (1992) [15]	5.486	5.585	3.772	2.914	0.296	0.011
Yasuda (1994) [16]	5.507	5.587	3.780	2.960	0.308	0.012
Herzinger (1998) [17]	5.531	5.632	3.773	2.942	0.286	0.009
Schinke(2015) [18]				2.908	0.326	0.011
Geist (1988) [21]		5.583	3.775		0.296	0.010
Green (2008) [23]	5.494	5.613	3.772	2.938	0.296	0.011
This work (2015)	5.498	5.595	3.770	2.924	0.304	0.011
Error	0.010	0.009	0.006	0.011	0.006	0.003
Average	5.500	5.597	3.773	2.927	0.301	0.011
Std. dev.	0.016	0.017	0.003	0.019	0.011	0.001
% error	0.3	0.3	0.1	0.6	3.6	9.1

edge), 400 nm (just below the direct band edge) and 700 nm (well below the direct band edge). Table 8.4 also shows the average values and the standard deviation from the average. Clearly, there is very little difference between the various data sets in the refractive index, where the % error is ~0.3%; we know the refractive index of silicon very well. There is considerably more error in the extinction coefficient, particularly when the extinction coefficient is small. This is an inherent limitation of ellipsometry measurements of small extinction coefficients, where it is more advantageous to use optical transmission measurements.

Acknowledgements GEJ acknowledges Oak Ridge National Laboratory for the use of facilities in the preparation of this manuscript. The work of PCJ was supported by the Department of Energy, Laboratory Directed Research and Development program at Oak Ridge National Laboratory, under contract DE-AC05-00OR22725.

References

1. W. Shockley, H.J. Queisser, J. Appl. Phys. **32**, 510 (1961)
2. W.C. Dash, R. Newman, Phys. Rev. **99**, 1151 (1955)
3. C.D. Salzberg, J.J. Villa, J. Opt. Soc. Am. **47**, 244 (1957)
4. W.G. Spitzer, H.Y. Fan, Phys. Rev. **106**, 882 (1957)
5. G.G. Macfarlane, T.P. McLean, J.E. Quarrington, V. Roberts, Phys. Rev. **111**, 1245 (1958)
6. H.R. Philipp, E.A. Taft, Phys. Rev. **120**, 37 (1960)
7. W. Primak, Appl. Opt. **10**, 759 (1971)
8. H.R. Philipp, J. Appl. Phys. **43**, 2835 (1972)
9. H.W. Icenogle, B.C. Platt, W.L. Wolfe, Appl. Opt. **15**, 2348 (1976)
10. H.A. Weakliem, D. Redfield, J. Appl. Phys. **50**, 1491 (1979)
11. G.E. Jellison Jr., D.H. Lowndes, Appl. Phys. Lett. **41**, 594 (1982)

12. G.E. Jellison Jr. in Ch. 3 of *Handbook of Ellipsometry*, ed. by H.G. Tompkins, E.A. Irene (William Andrew, Norwich, NY, 2005)
13. I.H. Malitson, J. Opt. Soc. Am. **55**, 1205 (1965)
14. D.E. Aspnes, A.A. Studna, Phys. Rev. B **27**, 985 (1983)
15. G.E. Jellison Jr., Opt. Mat. **1**, 41 (1992)
16. T. Yasuda, D.E. Aspnes, Appl. Opt. **33**, 7435 (1994)
17. C.M. Herzinger, B. Johs, W.A. McGahan, J.A. Woollam, W. Paulson, J. Appl. Phys. **83**, 3323 (1998)
18. C. Schinke, K. Bothe, P.C. Peest, J. Schmidt, R. Brendel, Appl. Phys. Lett. **104**, 081915 (2014)
19. C. Schinke, P.C. Peest, J. Schmidt, R. Brendel, K. Bothe, M.R. Vogt, I. Kroger, S. Winter, A. Schirmache, S. Lim, H.T. Nguyen, D. MacDonald, AIP Adv. **5**, 067168 (2015)
20. J. Geist, A. Migdall, H.P. Baltes, Appl. Opt. **27**, 3777 (1988)
21. J. Geist, in *Handbook of Optical Constants*, ed. by E.D. Palik (Academic Press, London, 1998)
22. M.J. Keevers, M.A. Green, Appl. Phys. Lett. **66**, 174 (1995)
23. M.A. Green, Sol. Energy Mater. Sol. Cells **92**, 1305 (2008)
24. P.Y. Yu, M. Cardona, *Fundamentals of Semiconductors: Physics and Materials Properties*, 3rd edn. (Springer, Berlin, 2005)
25. P. Lautenschlager, M. Garriga, L. Viña, M. Cardona, Phys. Rev. B **36**, 4821 (1987)
26. C.D. Thurmond, J. Electrochem. Soc. **122**, 1133 (1975)
27. G.E. Jellison Jr., F.A. Modine, Appl. Phys. Lett. **41**, 180 (1982)
28. G.E. Jellison Jr., F.A. Modine, Phys. Rev. B **27**, 7466 (1983)
29. G.E. Jellison Jr., H.H. Burke, J. Appl. Phys. **60**, 841 (1986)
30. G.E. Jellison Jr., F.A. Modine, J. Appl. Phys. **76**, 3758 (1994)
31. G.E. Jellison Jr., S.P. Withrow, J.W. McCamy, J.D. Budai, D. Lubben, M.J. Godbole, Phys. Rev. B **52**, 14607 (1995)
32. G.E. Jellison Jr., M.F. Chisholm, S.M. Gorbatkin, Appl. Phys. Lett. **62**, 3348 (1993)
33. P. Etchegoin, J. Kircher, M. Cardona, Phys. Rev. B **47**, 10292 (1993)
34. F.H. Pollak, Surf. Sci. **37**, 863 (1973)
35. G.E. Jellison Jr., D.H. Lowndes, Appl. Phys. Lett. **47**, 718 (1985)
36. G.E. Jellison Jr., D.H. Lowndes, Appl. Phys. Lett. **51**, 352 (1987)
37. K.D. Li, P.M. Fauchet, Solid State Commun. **61**, 207 (1987)
38. G.E. Jellison Jr., F.A. Modine, Appl. Phys. Lett. **69**, 371 (1996); ibid. 2137 (1996)
39. J. Tauc, R. Grigorovici, A. Vancu, Phys. Status Solidi **15**, 627 (1966)
40. A.S. Ferlauto, G.M. Ferreira, M. Pearce, C.R. Wronski, R.W. Collins, X. Deng, G. Ganguly, J. Appl. Phys. **92**, 2424 (2002)
41. G.D. Cody, in *Semiconductors and Semimetals*, vol. 21B ed. by J.I. Pankove (Academic, Orlando, FL, 1984), p. 11
42. G.E. Jellison Jr., V.I. Merkulov, A.A. Puretzky, D.B. Geohegan, G. Eres, D.H. Lowndes, J.B. Caughman, Thin Solid Films **377–378**, 68 (2000)
43. G.E. Jellison Jr., F.A. Modine, P. Doshi, A. Rohatgi, Thin Solid Films **313–314**, 193 (1998)
44. P. Doshi, G.E. Jellison Jr., A. Rohatgi, Appl. Opt. **36**, 7826 (1997)
45. M.F. Saenger, J. Sun, M. Schadel, J. Hilfiker, M. Schubert, J.A. Woollam, Thin Solid Films **518**, 1830 (2010)
46. E.A. Taft, L. Cordes, J. Electrochem. Soc. **126**, 131 (1979)
47. G.E. Jellison Jr., J. Appl. Phys. **69**, 7627 (1991)
48. C.M. Herzinger, B. Johs, W.A. McGahan, W. Paulson, Thin Solid Films **313–314**, 281 (1998)
49. B. Hoex, J. Schmidt, P. Pohl, M.C.M. van de Sanden, W.M.M. Kessels, J. Appl. Phys. **104**, 044903 (2008)
50. I.H. Malitson, M.J. Dodge, J. Opt. Soc. Am. **62**, 1405 (1972)
51. G.E. Jellison Jr., F.A. Modine, Appl. Opt. **36,** 8184 (1997); Appl. Opt. **36**, 8190 (1997)